# A study of temperature-related non-linearity at the metal-silicon interface.

P. M. Gammon,[1,2,3] E. Donchev,[2] A. Pérez-Tomás,[4] V. A. Shah,[3] J. S. Pang,[2] P. K. Petrov,[2] M. R. Jennings,[1] C. A. Fisher,[1] P. A. Mawby,[1] D. R. Leadley,[3] and N. McN. Alford[2]

[1)] *School of Engineering, University of Warwick, Coventry, CV4 7AL, United Kingdom*
[2)] *Department of Materials, Imperial College London, London, SW7 2AZ, United Kingdom*
[3)] *Physics Department, University of Warwick, Coventry, CV4 7AL, United Kingdom*
[4)] *IMB-CNM-CSIC, Campus UAB, 08193 Barcelona, Spain*

(Dated: 2 January 2013)

In this paper, we investigate the temperature dependencies of metal-semiconductor interfaces in an effort to better reproduce the current-voltage-temperature (I-V-T) characteristics of any Schottky diode, regardless of homogeneity. Four silicon Schottky diodes were fabricated for this work, each displaying different degrees of inhomogeneity; a relatively homogeneous NiV/Si diode, a Ti/Si and Cr/Si diode with double bumps at only the lowest temperatures, and a Nb/Si diode displaying extensive non-linearity. The 77-300 K I-V-T responses are modelled using a semi-automated implementation of Tung's electron transport model, and each of the diodes are well reproduced. However, in achieving this, it is revealed that each of the three key fitting parameters within the model display a significant temperature dependency. In analysing these dependencies, we reveal how a rise in thermal energy "activates" exponentially more interfacial patches, the activation rate being dependent on the carrier concentration at the patch saddle point (the patch's maximum barrier height), which in turn is linked to the relative homogeneity of each diode. Finally, in a review of Tung's model, problems in the divergence of the current paths at low temperature are explained to be inherent due to the simplification of an interface that will contain competing defects and inhomogeneities.

PACS numbers: Valid PACS appear here
Keywords: Suggested keywords

## I. INTRODUCTION

Schottky barriers, formed at the interface between a metal and a low-doped semiconductor, are the simplest of electronic phenomena and occur in numerous devices. Most obvious is the Schottky diode which, compared with a semiconductor-semiconductor diode such as a *PiN* diode, has very fast switching speeds and low turn-on voltages due to its reliance only on majority carrier transport, free of the recombination mechanism. This makes the Schottky diode a popular choice in applications such as switched mode power supplies, RF, voltage clamping, and now extensively also in power electronics, where the latest silicon carbide (SiC) Schottky diodes from Cree are capable of blocking voltages up to 1700 V[1]. Schottky barriers also find use as the gate of high electron mobility transistors (HEMT), where one of the most popular combinations is AlGaN/GaN, with the Schottky barrier being formed to the GaN top layer[2–4], though many other III-V combinations have been suggested[5]. Other applications include carbon nanotube Schottky barrier transistors[6], and Schottky solar cells, with materials including lead selenide nanocrystals[7] and graphene[8].

Despite over a hundred years of research and development into Schottky barriers, across all popular semiconductors and for the various applications, we still find ourselves with unanswered questions as to the nature of current flow across the barrier, especially in light of inhomogeneity at the metal-semiconductor interface[9,11–24], which can result in multiple conduction paths through the non-uniform interface. Sources of interfacial inhomogeneity include processing remnants (dirt, contamination), surface roughness, native oxide, an uneven doping profile, crystal defects and grain boundaries[9,11,12] and it is generally now accepted that the surface is better represented as a random array of different patches, each of varying barrier height and area, as represented in the inset of Figure 1a.

The thermionic emission equation has long since been used to model the turn-on characteristics of Schottky diodes, and predicts that as a diode turns on, it will have a linear response on a semi-log plot with an ideality factor, $\eta$, approaching 1. The thermionic emission equation is,

$$I = AA^*T^2 \exp\left(-\beta\Phi\right)\left[\exp\left(\beta V_A/\eta\right) - 1\right], \qquad (1)$$

where $A$ represents the contact area, $A^*$ is the Richardson constant, $T$ is the temperature, $\Phi$ is the Schottky barrier height, $V_A$ is the applied voltage and $\beta = q/k_bT$, with $q$ the electron charge, and $k_b$ the Boltzmann constant. Interfacial inhomogeneity has been cited[9–24] as the cause for many experimental results that deviate from this response. These so called *non-linearities* include high ideality factors[9,11,13], the discrepancy between Schottky barrier heights (SBH) extracted via CV and IV techniques[9–15], the "$T_0$ anomaly"[9,11,13], double bumps within the semi-log turn-on characteristics[9,11,13,16–20], edge effects[9,11] and non-linearity within Richardson plots[22].

It was the papers written by Tung[9–11] however, that first introduced a model that adapted Equation 1 to fully explain the non-linearities in light of interfacial inhomogeneity and SBH fluctuation. Tung built on the work of those that had proceeded him[13–15] by basing his model

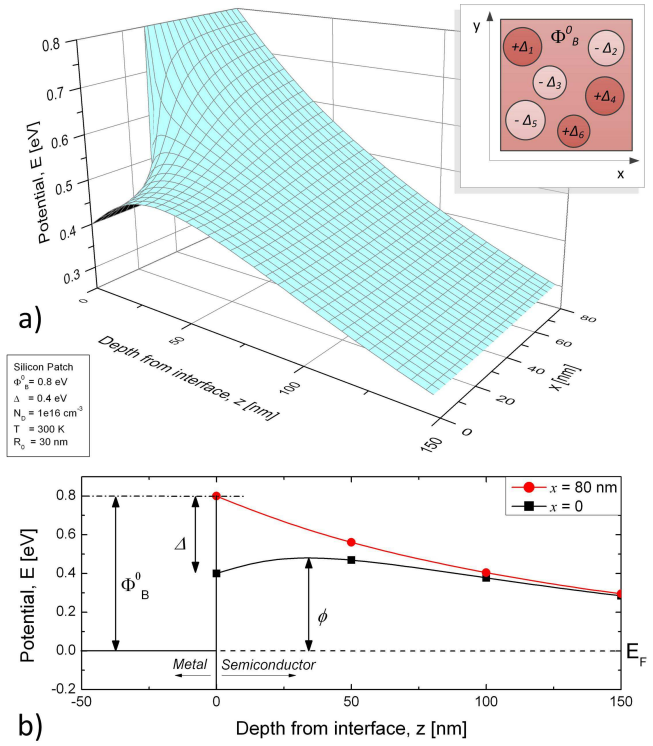


FIG. 1. a) A 3-dimensional representation of SBH pinch off in a silicon patch. The saddle point is 30 nm into the Si from the interface. This is a reproduction of Figure 5 of Tung's Theory[9]. Inset: A two dimensional representation of the interface as it is modelled herein, with its patches of varying size and barrier heights. b) Conventional band diagrams taken from the same interface, showing some of the parameters used herein.

on an interface with a Gaussian array of barrier heights. However, Tung formalised for the first time the idea that an area, or patch, with a low barrier may be obscured by those areas of larger barrier height that surround it, the idea of SBH pinch off. This lead us away from the idea generated previously[13] that an inhomogeneous interface can be modelled as the sum of several micro-diodes in parallel, each with its own barrier height. Instead, consider the situation of Figure 1 where there is a uniform region that has the barrier height ($\Phi^0_B$), in which there is a single patch with a low barrier height ($\Phi^0_B - \Delta$). Pinch off is the notion that $\Phi^0_B - \Delta$ will not be the lowest energy level that a carrier will have to reach on its conduction path from the semiconductor bulk into the metal. As you move away from the metal-semiconductor interface towards the bulk, the high and low energy levels that are so separate at the interface must meet and flatten out before reaching the flat-band bulk conditions. This leaves a potential hill, or saddle-point at an energy $\phi$ above the Fermi level ($E_F$), some tens of nanometres into the semiconductor that is higher than $\Phi^0_B - \Delta$.

Tung states[9] that at low temperature, Ohmic effects within the few conducting patches cause the dual current paths to become deconvoluted. This might explain the frequently cited and debated double bumps that can be seen variously in Si Schottky diodes[9,11], SiC diodes[16–20], GaAs diodes[23,24], and also in heterojunctions[12,25]. The worsening of these effects in devices without guard rings or other edge protection, could futher be explained by low SBH patches at the device extremities which are not pinched off as well as those in the centre of the device, these being surrounded on all sides by the higher background patches[9–11]. This pinch-off effect can also explain ideality factors greater than 1, with the height of the saddle point being in turn dependent on the band-bending potential and hence the applied voltage. As more voltage is applied, the minimum barrier energy is actually raising, causing the illusion of a more shallow thermionic emission slope.

In this paper, we rigorously test Tung's original analytical model by using modelling techniques to reconcile the model (derived and explained in Appendix A) with real I-V-T data, taken from Schottky diodes of varying homogeneity. This is something that was not carried out in the original work[9], and in doing so, we will show that there are further temperature dependencies inherent within the model's fitting parameters which, when taken into account, allow a very good agreement to be reached between the two. The four metal-Silicon Schottky interfaces have nickel-vanadium (NiV), titanium (Ti), chromium (Cr) and niobium (Nb) as contact metals and for each of these diodes, this will be the first time they have been characterised in this fashion. The four diodes represent three different degrees of homogeneity, the NiV diode showing almost no non-linearity, whilst the Nb diode contains large ideality factors and double bumps most of the way to room temperature. Both the Ti and Cr diodes sit between these two extremes.

## II. EXPERIMENTAL DETAILS

Lateral Schottky diodes were produced on n-type silicon. A three mask process was employed to form lateral devices on highly n-doped ($1.2 \times 10^{19}$ cm$^{-3}$) (100) Si substrates with a 2 $\mu$m lightly phosphorous doped ($1 \times 10^{16}$ cm$^{-3}$) epitaxial layer. After standard RCA cleaning, an initial 3 $\mu$m CF4-plasma etch in a Sentech Etchlab 200 Reactive Ion Etcher created mesa structures and exposed the higher doped substrate. The diodes' cathodes were then formed by sputtering Ti on the exposed and roughened highly doped surface before being placed in a Heatpulse 610 rapid thermal annealing system for 30 seconds at 800 °C in argon ambient. The different top-contact metals could then be sputtered onto the mesa surface using a Mantis QPrep Deposition System. The final structure can be seen in the inset of Figure 2. These devices were characterised using standard current-voltage techniques (I-V) in a vacuum and at temperatures ranging from 77 to 300 K. Capacitance-Voltage (C-V) measurements were also carried out at room tempera-

ture. Lateral devices were formed to make wire bonding to these structures easier when it came to IVT testing. As seen in the inset of Figure 2, the mesa etch accurately defines the drift region between the metal and the homojunction. On the application of a negative voltage (to a maximum of -5 V for the C-V measurements), the depletion region will never exceed the width of the drift region, so the devices are presumed to operate in the same fashion as conventional vertical devices for both CV and IV analysis.

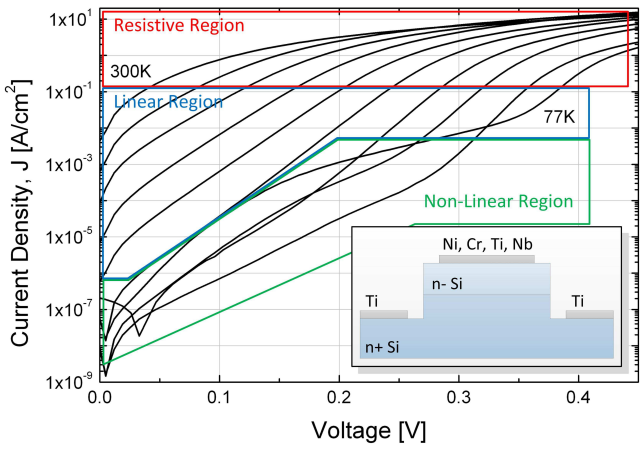


FIG. 2. A typical I-V-T response from a Cr/Si Schottky diode. A 77 K minimum temperature is shown and then 25 K intervals from 100 K to 300 K. The resistive region is never reproduced throughout. The temperature independent Tung model is capable of reproducing only the linear region, while the temperature dependent model can model both the linear and non-linear regions. Inset: The structure of the Schottky diodes formed within this work.

The four diodes selected for this work were chosen because of their varying degrees of inhomogeneity, with the NiV diode producing the most homogeneous response with ideality factors ranging from 1.056 at 300 K to 1.378 at 100 K, and minimal bumps or kinks down to 77 K. Both the Cr diode shown in Figure 2, and the Ti diode displayed severe double bumps at 77 K but was reasonably linear at temperatures above 150 K. Showing a great deal of non-linearity, the Nb diode had very high ideality factors, and extensive double bumps all the way up to room temperature.

Figure 2 shows a typical set of experimental results from one Cr/Si Schottky diode. Three distinct regions typically form, as highlighted in the Figure. Plotted in a semi-log format, a linear region, typically modelled by the diode equation, is between a resistive region and a non-linear region, which at lower temperature contains the afore-mentioned double bumps. In setting up the fitting program, it was decided to ignore the resistive region (typically above 0.1 A/cm$^2$) altogether as it is quite predictable and irrelevant to the current investigation. The program developed could simulate one or more I-V responses across either the linear region of a semi-log plot, or the entire linear and non-linear portions. A rigorous and efficient method of fitting was produced whereby an algorithm would search through a predefined range for each of the three fitting parameters, using a coefficient of determination, $R^2$, to determine which combination of parameters led to the best fit. This is defined in Appendix B.

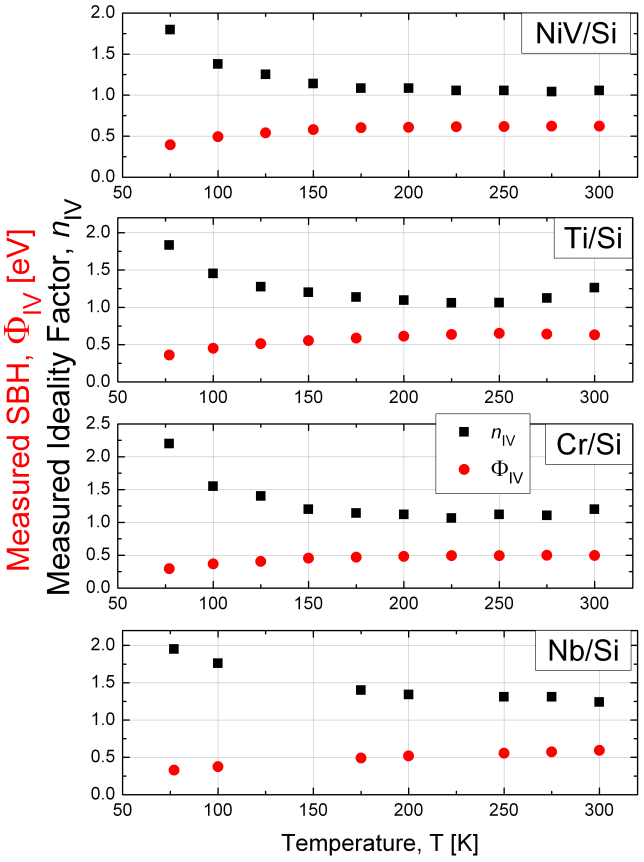


FIG. 3. A typical set of barrier heights and ideality factors extracted over the full temperature range for the four Schottky diodes.

## III. RESULTS AND DISCUSSION

As a starting point, we applied conventional analysis (see for example[27]) on each of the I-V responses using Equation 1 to extract temperature dependent ideality factors ($\eta_{IV}$) and barrier heights ($\Phi_{IV}$). Figure 3 shows all the collated results, except for those from the Nb diode profile where the extreme double bumps prevented such an approach. Typical characteristics are seen as reported for various other diodes[13,22], whereby $\Phi_{IV}$ increases, and $\eta_{IV}$ decreases, with temperature, until at higher temperatures the series resistance skews the extracted values of $\eta_{IV}$, as seen in the Cr response of Figures 2 and 3.

The minimum $\eta_{IV}$ will be at different temperatures for different diodes, depending on barrier height, series resistance and relative homogeneity. Therefore, in listing the best I-V results in Table I, for fair comparison, the results listed are at the $\eta_{IV}$ minima, with the measurement temperature $T_{IV}$ also listed. The ideality factors give a first indication of the quality of each diode, the NiV, Ti and Cr diodes each with $\eta_{IV} < 1.1$, but the Nb diode displays significant signs of inhomogeneity with a best value of 1.24. For completeness, Table I shows the SBHs extracted via C-V characterisation at room temperature. These barrier heights were higher than those extracted via I-V characterisation at room temperature (not shown) in all but the Nb diode. This has often been shown to be the case[9–15], as C-V characterisation tends to characterise the average barrier height across an interface, whereas with I-V characterisation, current takes the path of least resistance, such that patches of low barrier height will preferentially conduct first.

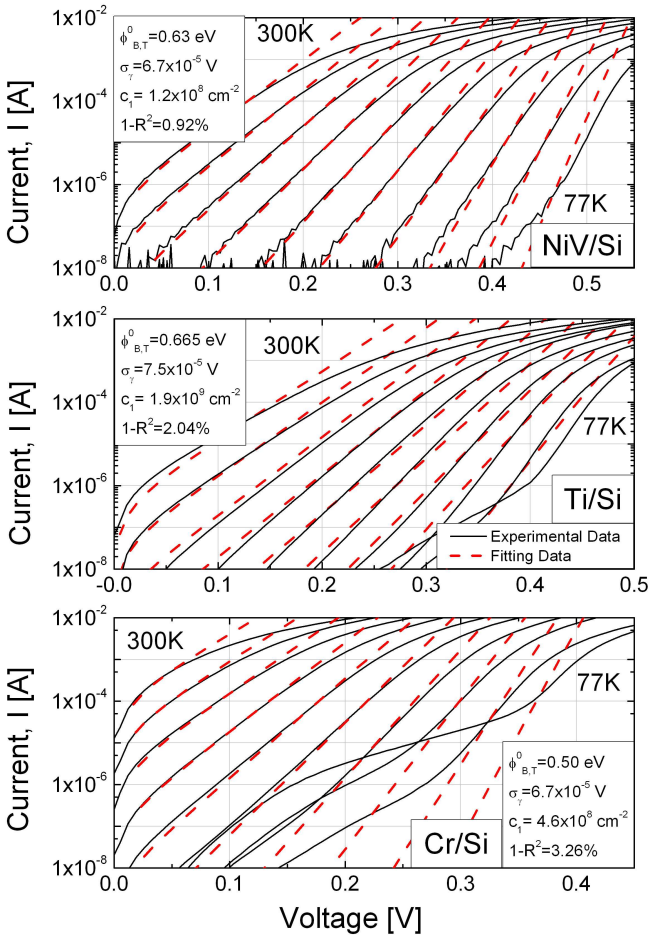


FIG. 4. I-V-T responses from the NiV, Ti and Cr Schottky diodes. The best fits achieved using temperature independent fitting parameters are shown.

The full Tung model is derived in Appendix A, leading to the model used herein, Equation A9. Very little has been reported about the relationship between temperature and the fitting parameters $C_1$, $\sigma_\gamma$, and $\Phi_B^0$ of this model. Tung[9] provided examples of his model over similar temperature ranges to those considered here, always using a fixed set of parameters, but without ever fitting these to experimental data. Hence, in a first attempt to simulate the experimental data here, we attempted to minimise $1 - R^2$ using a set of $C_1$, $\sigma_\gamma$, and $\Phi_B^0$ values that were also fixed over the entire temperature range. However, it was soon discovered that fixing $C_1$ and $\sigma_\gamma$ made it impossible to model the non-linear region shown in Figure 2 because the values required to fit to the low temperature non-linearities would skew the linear, higher temperature responses. Figure 4 shows the best fits from the NiV, Ti and Cr/Si Schottky diodes, whilst Table II summarises the fitting parameters and the best $1 - R^2$ values attained for these diodes. The Nb diode could not reasonably be fit using fixed variables, its extensive double bumps, requiring vastly different fitting parameters at each temperature. Of the other diodes, the best fits employed a patch coverage ($C_P$) of around 1-3% to increase the ideality factors of the middle and lowest temperatures, whilst at high temperatures the background current dominated. No single combination could do all this and incorporate the double bumps, as a different $C_1$ and $\sigma_\gamma$ combination was necessary for each low-temperature I-V plot.

| | | NiV | Ti | Cr | Nb |
|---|---|---|---|---|---|
| $\Phi_{CV}$ | (eV) | 0.705 | 0.866 | 0.543 | 0.589 |
| $\Phi_{IV}$ | (eV) | 0.621 | 0.639 | 0.494 | 0.593 |
| $\eta_{IV}$ | | 1.042 | 1.059 | 1.065 | 1.240 |
| $T_{IV}$ | (K) | 275 | 225 | 225 | 300 |

TABLE I. SBH ($\Phi$) and ideality factors ($\eta$) from conventional C-V (at 300 K) and I-V extraction is shown. The I-V results are taken from where $\eta_{IV}$ is at its minimum value across the temperature range, hence the measurement temperature is also shown.

Clearly a temperature independent model is inaccurate despite having some success with the more homogeneous responses. Hence, a new approach was investigated whereby the optimum fitting parameters were found at every temperature interval, allowing us to observe the temperature dependence of each of the parameters within the model. Therefore, a $1-R^2$ minimisation now took place at every temperature interval and hence it could incorporate both the linear and non-linear regions of the diode response. Figure 5 shows that a good fit was achieved for all four diodes, including the unpredictable and inhomogeneous Nb/Si diode.

The temperature dependent approach results in very good fits, but one is left with a database of fitting parameters across diode types and temperature intervals. Hence, we have plotted $C_1$, $\sigma_\gamma$, and $\Phi_B^0$ against temperature, shown in Figure 6, and over the next three

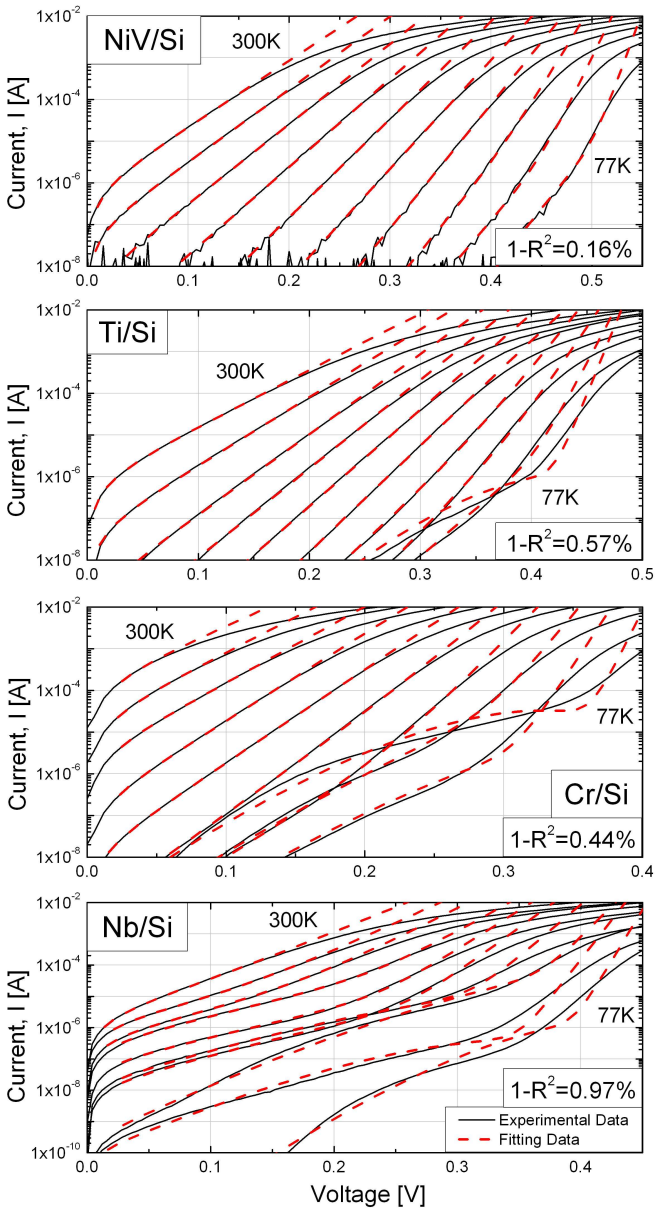


FIG. 5. I-V-T responses from the four Schottky diodes. The best fits achieved for each using free, temperature dependent fitting parameters are shown.

sections we shall attempt to explain the temperature related trends within the framework of the model, relating them back to a physical meaning and probing at the validity of the Tung model in light of this new data. To this end, we have also reproduced in Figure 6d the $1-R^2$ fitting data, which indicates how the accuracy of the model deteriorates with decreasing temperature. This is visually evident from Figure 5, in particular within the Cr/Si diode, and it is clear that while the model has an ability to mimic the shape of the worst non-linearities, the most accurate fits come as the non-linearities begin to disappear with increasing temperature. All three of the

| | | NiV | Ti | Cr | Nb |
|---|---|---|---|---|---|
| | | $T$ Independent Parameters | | | |
| $\Phi_B^0$ | eV | 0.63 | 0.665 | 0.503 | n/a |
| $\sigma_\gamma$ | $\mu$eV | 42 | 75 | 67 | |
| $C_1$ | cm$^{-2}$ | $1.59\times10^{10}$ | $1.85\times10^{9}$ | $4.62\times10^{8}$ | |
| $1-R^2$ | % | 2.54 | 2.04 | 3.26 | |
| | | $T$ Dependent Parameters | | | |
| $1-R^2$ | % | 0.16 | 0.57 | 0.44 | 0.97 |
| $T_p^0$ | K | 160 | 224 | 272 | 664 |
| $\sigma_T$ | K | 19.1 | 22.9 | 30.2 | 91.2 |
| $\Phi_{B,0}^0$ | eV | 0.629 | 0.506 | 0.459 | 0.493 |
| $m_{\Phi,T}$ | $\mu$eV/K | 108 | 787 | 262 | 494 |
| $\sigma_{\gamma,0}$ | $\mu$eV | 123 | 148 | 154 | 109 |
| $m_{\sigma\gamma,T}$ | neV/K | -505 | -523 | -461 | 74 |
| $\Phi_{P,0}^0$ | eV | 0.614 | 0.652 | 0.606 | 0.694 |
| $m_{\Phi,V}$ | meV/V | 35 | 9 | -84 | 215 |
| $\sigma_{\Phi,0}$ | meV | 61 | 78 | 86 | 101 |
| $m_{\sigma,V}$ | meV/V | -72 | -92 | -133 | -95 |
| $n_{\Phi 0}$ | cm$^{-3}$ | $5.66\times10^{-1}$ | $4.51\times10^{4}$ | $2.28\times10^{8}$ | $5.74\times10^{14}$ |

TABLE II. A summary of all the parameters extracted from the fitting of the Tung model to the real silicon Schottky diodes.

parameters display some temperature dependence and in Figure 6b) and c) is a line of best fit through each of the fitting parameters, with Table II displaying the slope and intercept values for each of these.

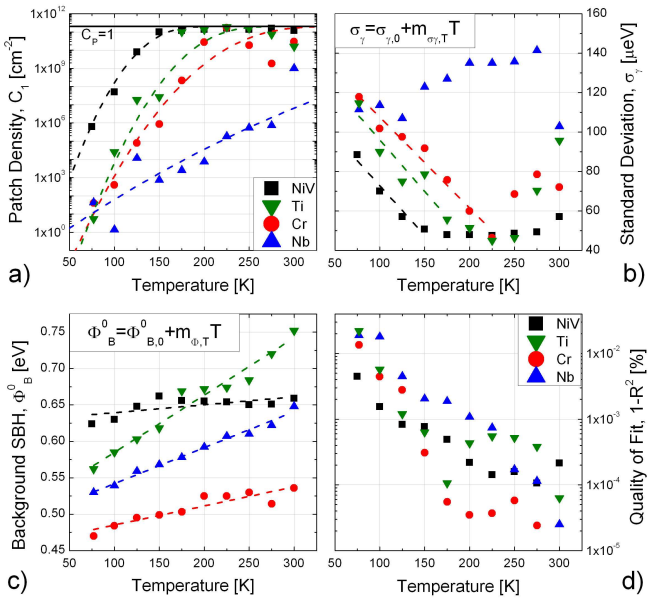


FIG. 6. A typical set of fitting parameters extracted from each of the NiV, Ti, Cr, and Nb silicon Schottky diodes.

### A. The temperature dependence of $C_1$

The most significant result in Figure 6 is that of $C_1$, which has an exponential temperature dependence in all four of the diodes. We can see from Figure 6a that the Ti diode, for example, is modelled having less than 10 patches per cm$^2$ at the lowest temperature, rising to $2 \times 10^{11}$ cm$^{-2}$ by 200 K, where the patch density is limited as $C_p$ (the total patch area as a percentage of contact area) tends to 1 (or $C_1 A_{\text{eff}} \rightarrow A$). $C_1$ in particular can no longer be described as temperature independent and its previous definition[9,21] as the total density of patches at the interface should change. In light of this evidence, it seems more accurate to describe it as the number of *active*, conducting, patches per unit area at a given temperature. Indeed, given that the Tung model, like those that preceded it, still incorporates a Gaussian distribution of barrier heights (albeit tied in with the patch size $R_0$ within the patch parameter $\gamma$), this relationship is easily visualised; at a low temperature, a small number of free carriers will exist within the conduction band, which, given an applied voltage, will have enough energy to activate a small percentage of patches up to a maximum barrier height (the saddle point, or $\phi$ in Figure 1b) at the lowest end of the energy distribution. Raise the temperature, and more carriers will be induced into the conduction band or, another way to look at it; the same number of carriers will be available at a higher energy, and hence the number of active patches will rise exponentially according to the original Gaussian distribution. Removing $R_0$ from the patch parameter, $\gamma$, this scenario is represented in Figure 7a, where an imaginary patch energy distribution following the PDF equation of Equation A2 is shown with a mean patch barrier height $\Phi_P^0 = 0.55$, and a corresponding standard deviation $\sigma_\phi = 0.07$. Also shown is a cumulative distribution function (CDF), which is defined, in general for the Gaussian distribution of Equation A1, $f\left[x;\mu,\sigma^2\right]$, as,

$$F\left[x;\mu,\sigma^2\right] = \int_{-\infty}^{x} f\left[x;\mu,\sigma^2\right] dx = \frac{1}{2}\left[1 + \text{erf}\left(\frac{x-\mu}{\sigma\sqrt{2}}\right)\right] \quad (2)$$

The distribution in Figure 7a is therefore,

$$C_1 \approx C_{1,\text{Tot}} F\left[\phi;\Phi_P^0,\sigma_\phi^2\right], \quad (3)$$

where $C_{1,\text{Tot}}$ is determined from the Tung model as the total number of patches that are active as $C_P$ tends to 1 and is here $2 \times 10^{11}$ cm$^{-2}$, as seen in Figure 6a. Hence, in Figure 7a, two points representing two different temperatures (where $T_1 < T_2$) are marked on the CDF. The temperature rise between the two points raises the active patch energy, $\phi_{\max}$, by 0.1 eV, which in this scenario raises the number of active patches per unit area by an order of magnitude.

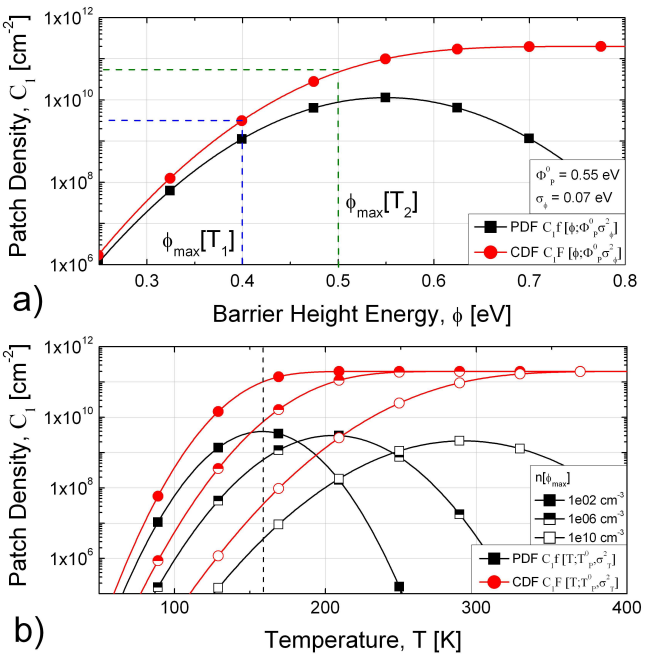


FIG. 7. a) A Gaussian distribution of patch barrier heights represented using a PDF and CDF distribution. b) The energy distribution of a) transformed through Equation 4 using three values of $n[\phi_{\max}]$. The result shows how the activation temperature of the average barrier height may be manipulated.

The above scenario could justify the exponential increase of the fitting parameter $C_1$ with temperature, as it follows a CDF profile. Therefore, if we state that a minimum carrier concentration ($n[\phi_{\max}]$) is required to activate all those patches with a saddle point energy $\phi < \phi_{\max}$, then the relationship between temperature and $\phi_{\max}$ (measured from the Fermi level) can be described by substituting these values into Equation A6 and rearranging,

$$\phi_{\max} = -\frac{kT}{q} \ln\left(\frac{n[\phi_{\max}]}{N_C}\right). \quad (4)$$

Over the temperature ranges considered here, the temperature dependence of $N_C$ has a negligible effect on $\phi_{\max}$, and the relationship between $\phi_{\max}$ and $T$ can be considered linear. A problem arises however; if the carrier concentration required to activate a patch ($n[\phi_{\max}]$) were constant across all the Si diodes, then the metal-semiconductor interface with the lowest average barrier height would always be the one to reach saturation first. We have seen from Figure 6a that this is not the case with the relatively homogeneous NiV diode ($\Phi_{IV} = 0.621$ eV) reaching $C_p$ saturation at a lower temperature than the Cr ($\Phi_{IV} = 0.494$ eV) or Ti diodes ($\Phi_{IV} = 0.639$ eV), whilst the Nb diode ($\Phi_{IV} = 0.593$ eV) which suffers the many double bumps, does not reach this mark before 300 K.

We therefore propose that $n[\phi_{\max}]$ is not the same for every diode, and as such we here treat it as a variable that is strongly influenced by the homogeneity of the contact, with a low value meaning that all the patches will become active at a low temperature, as in the NiV diode. This idea is demonstrated in Figure 7b, where the energy distribution of Equation 3 and Figure 7a, $\mathrm{F}\left[\phi;\Phi_P^0,\sigma_\phi^2\right]$, has been transformed through Equation 4 using three different values of $n[\phi_{\max}]$, to get,

$$C_1 \approx C_{1,\mathrm{Tot}} F\left[T;T_P^0,\sigma_T^2\right]. \tag{5}$$

Figure 7b shows clearly how the temperature response will spread, the corresponding values of $T_P^0$ and $\sigma_T$ being greatly affected by the size of $n[\phi_{\max}]$. Given the lowest value of $n[\phi_{\max}]$ shown, $1\times10^2$ cm$^{-3}$, the average patch of the distribution in Figure 7a will be activated by 159 K, the large number of conducting patches at this temperature meaning that the I-V response will be linear. At the larger $n[\phi_{\max}]$ of $1\times10^{10}$ cm$^{-3}$, nearly 3000 times fewer patches will have been activated by 159 K, and the response at this temperature may well display kinks. The average patch of this distribution would not be activated until 300 K.

For the four diodes shown in Figure 6a, using another $1-R^2$ minimisation, it was possible to fit Equation 5 to the temperature dependent parameters that were extracted from the I-V-T modelling. Hence, for each diode, the best fit is shown in the Figure, with the values of $T_p^0$ and $\sigma_T$ summarised in Table II. It can be seen that the values for the Nb diode far exceed that of the Cr and NiV diodes, which suggest that this diode may require a large $n[\phi_{\max}]$ value to activate it patches.

### B. The temperature dependence of $\sigma_\gamma$

As with the fitting parameter $C_1$, the original Tung model[9,11] offers no explicit mention of a $\sigma_\gamma$ temperature dependence, however Equation 24 of Tung's model[9] relates $\sigma_\gamma$ to the ideality factor, expanded here as:

$$n \approx 1+\frac{\sigma_\gamma^2 V_{bb}^{2/3}}{3\beta\eta^{2/3}}. \tag{6}$$

This relationship provides a direct link between the standard deviation of the patch parameter and the ideality factor profiles of Figure 3, explaining why, in general, the value of $\sigma_\gamma$ seen in Figure 6b decreases with temperature before rising again at higher temperatures as series resistance begins to skew the I-V profiles. This is particularly true of the Ti/Si diode, where the temperature responses of $n_{IV}$ within Figure 3, and $\sigma_\gamma$ in Figure 6b look very similar.

As far as modelling the $\sigma_\gamma$ profiles within Figure 6b and finding a temperature related trend, it appears that all the profiles except the Nb diode follows a pattern similar to the $C_1$ profiles, reaching a minimum value of around 45 $\mu$eV as $C_P$ tends to 1. Prior to this, the three diodes all appear to have approximately the same negative slope as indicated with the linear fits shown. It is worth mentioning here that both the $\sigma_\gamma$ and $C_1$ profiles of the Ti and Cr diodes are somewhat skewed at high temperature where, unlike the NiV diode, the two diodes are influenced by series resistance. In Figure 8 we show the full extent of the correlation between $\sigma_\gamma$ and $C_1$, plotting these two parameters against each other for every temperature point. The line of best fit through the data in Figure 8 relates $\sigma_\gamma$ and $C_1$, ignoring the Nb data and those aforementioned data points that are heavily influenced by series resistance. The fit approximately follows:

$$C_1 = C_0\exp\left(-m_{C\sigma}\sigma_\gamma\right). \tag{7}$$

where in Figure 8, $C_0 = 2.333\times10^{18}$ and $m_{C\sigma} = 3.341\times10^5$. What this would mean physically is that as temperature rises, exponentially more patches are becoming active whilst at the same time the distribution of $\gamma$ is narrowing, though a reason for this is unclear, perhaps due to the reduction in patch barrier height with temperature, or a relationship between $R_0^2$ and temperature. Whatever the reason, if we use the relationship seen in Figure 8, then the parameter $\sigma_\gamma$ becomes predictable using the same mechanisms (Equations 3-5) that determined $C_1$.

Also shown in Figure 8 is the difference between those diodes that visually appear to be linear (hollow shapes), and those that display kinks or double bumps (filled shapes). A cut off appears evident, especially in the patch density, whereby any response with $C_1 < 10^8$ cm$^{-2}$ displaying some non-linearity. The further any individual I-V response is towards the bottom-right of Figure 8, the greater the double bump appears in Figure 5.

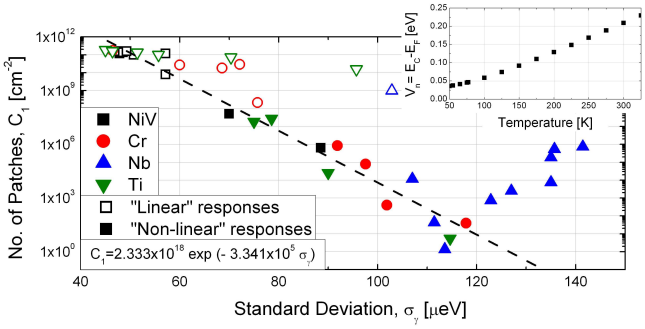


FIG. 8. The fitting parameters $C_1$ and $\sigma_\gamma$ from all the I-V responses plotted in Figure 5. Highlighted are those that visually display non-linearities: kinks or double bumps. The line of best fit ignores the Nb diode and those influenced by series resistance. Inset: the temperature dependence of $V_n$, as determined from Equations A6 and A7

The diodes' $\sigma_\gamma$ vs. temperature profiles, perhaps more than any of the others, shows how hard it is to simulate the most inhomogeneous diodes. The ideality factors of

the Nb/Si profile were taken from the linear regions of the profile, above the double bumps, and hence the Nb ideality factor profile in Figure 3 does not correlate with the very large values of $\sigma_\gamma$ in Figure 6b. For this Nb diode, there is little definitive correlation between $C_1$ and $\sigma_\gamma$, whilst in Figure 6b, we see a positive correlation between $\sigma_\gamma$ and temperature and these large values of $\sigma_\gamma$, combined with the low values of $C_1$ lead to the profile full of double bumps up to 275 K seen in Figure 5. Given the evidence above linking $\sigma_\gamma$ to both $C_1$ and the experimental ideality factors, it is questionable whether a diode with this degree of non-linearity may be modelled in the same fashion.

### C. The temperature dependence of $\Phi_B^0$

$\Phi_B^0$ had previously been presumed to be stable across the temperature range[9,11]. However, the fitting carried out here could not have been completed with a fixed $\Phi_B^0$, and Figure 6c displays the temperature dependence, and in general a positive, linear correlation over the temperature range is observed such that,

$$\Phi_B^0 = \Phi_{B,0}^0 + m_{\phi,T}T. \tag{8}$$

This in itself is not surprising given the temperature dependence of $V_n$ ($V_n = E_C - E_F$), which is shown in the inset of Figure 8. Interfacial traps within the semiconductor bandgap causes the Fermi level of most semiconductors to be pinned at its surface[25,28,29]. This causes band bending to occur at the surface, prior to contact with the metal, weakening the link between the Schottky barrier height and the work function offset, as laid out by the Schottky-Mott principle. This means that the magnitude of $V_n$ directly influences the size of the barrier height and its positive correlation with temperature, as seen in the inset of Figure 8, will cause an increase of barrier height with temperature.

### D. The influence of carrier concentration $n[\phi_{\max}]$ on the Tung model.

In the previous sections, we have shown how the three parameters that make up the Tung model are themselves related to temperature. In Figure 7, we showed how the temperature dependent values of $C_1$ can be extracted from an initial Gaussian distribution of maximum patch barrier heights ($C_{1,\mathrm{Tot}} f\left[\phi; \Phi_P^0, \sigma_\phi^2\right]$) using Equation 4, with the carrier concentration at a patch's minimum barrier height, $n[\phi_{\max}]$, determining how homogeneous that response will be. Having also defined the parameters $\sigma_\gamma$ and $\Phi_B^0$, we can now complete a full simulated example of an I-V-T plot to show the influence that $n[\phi_{\max}]$ has on a generic interface, making the difference between a homogeneous response and one with extensive non-linearities.

Figure 9 shows 13 simulated I-V responses ranging in temperature from 75 K to 375 K using the three different values of $n[\phi_{\max}]$ introduced in Figure 7, $1\times10^2$, $1\times10^6$ and $1\times10^{10}$ cm$^{-3}$. Each of the 13 temperature values, of which three are shown in Table III, were entered into Equation 4 to find the energy, $\phi_{\max}$, at which a carrier concentration of $n[\phi_{\max}]$ will exist. Then, $C_1$ - the number of active patches with a barrier height equal to or less than $\phi_{\max}$ - could be found using the CDF of Equation 3. We presumed that the barrier height distribution is temperature dependent and hence, we made $\Phi_P^0 = \Phi_B^0$, however, a consistent standard deviation is used with $\sigma_\phi = 0.07$. This linear relationship between $\Phi_B^0$ and temperature was determined using a value of $\Phi_{B,0}^0$ equal to 0.55 eV, and $m_{\phi,T} = 0.108$ $\mu$eV/K - the same as the NiV diode. The linear relationship determined between $C_1$ and $\sigma_\gamma$ in Figure 8 was used to extract $\sigma_\gamma$ for each value of $n[\phi_{\max}]$. Having generated the full set of fitting parameters including those examples shown in Table III, these were entered into the Tung model of Equations A9 to A13 to produce the I-V-T responses shown in Figure 9.

In Figure 9a, we see a reasonably homogeneous response, the low value of $n[\phi_{\max}]$ having translated the original Gaussian distribution shown in Figure 7a into a response that is free of kinks in all but the lowest simulated temperature. This profile is repeated in each of the other two profiles to illustrate the increasing inhomogeneity at low temperatures. The double bumps clearly stand out, as do the barrier heights, which appear to increase with $n[\phi_{\max}]$, as seen in b) and c) of Figure 9. This is further illustrated in Figure 10, where the ideality factors (taken as an average of the entire response, including the double bumps) and SBHs of the simulated example are extracted via the traditional methods[27] that use Equation 1.

| | | I-V Temperature [K] | | |
|---|---|---|---|---|
| | | 100 | 200 | 300 |
| $\Phi_B^0 = \Phi_P^0$ | eV | 0.561 | 0.572 | 0.582 |
| $\phi_{\max}[1e02]$ | eV | 0.333 | 0.684 | 1.042 |
| $\phi_{\max}[1e06]$ | eV | 0.254 | 0.526 | 0.804 |
| $\phi_{\max}[1e10]$ | eV | 0.175 | 0.367 | 0.566 |
| $C_1[1e02]$ | cm$^{-2}$ | $1.1\times10^{8}$ | $1.9\times10^{11}$ | $2.0\times10^{11}$ |
| $C_1[1e06]$ | cm$^{-2}$ | $1.2\times10^{6}$ | $5.1\times10^{10}$ | $2.0\times10^{11}$ |
| $C_1[1e10]$ | cm$^{-2}$ | $3.4\times10^{3}$ | $3.4\times10^{8}$ | $8.1\times10^{10}$ |
| $\sigma_\gamma[1e02]$ | $\mu$eV | 71.0 | 48.9 | 48.7 |
| $\sigma_\gamma[1e06]$ | $\mu$eV | 84.8 | 52.8 | 48.7 |
| $\sigma_\gamma[1e10]$ | $\mu$eV | 102 | 67.8 | 51.4 |

TABLE III. A snapshot of three of the temperature dependent parameters used to produce the I-V-T simulations of Figure 9.

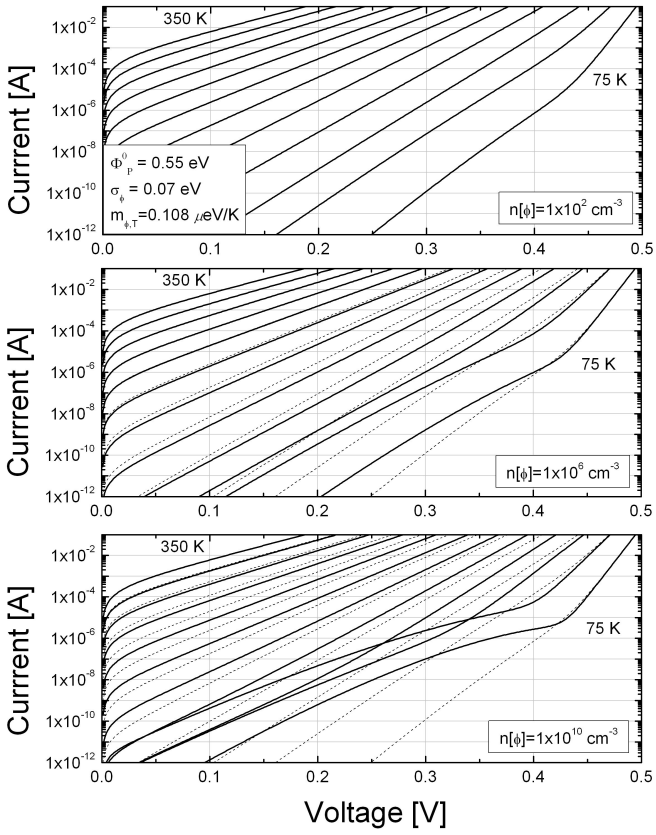


FIG. 9. Simulations that use the equations developed in this paper to illustrate the link between $n[\phi_{\max}]$ and homogeneity, following on from the example begun in Figure 7. The value of $n[\phi_{\max}]$ used within Equation 4 was the only difference between the three responses shown. The dotted lines in b) and c) are the profile from a) repeated in order to highlight the non-linearities in these responses.

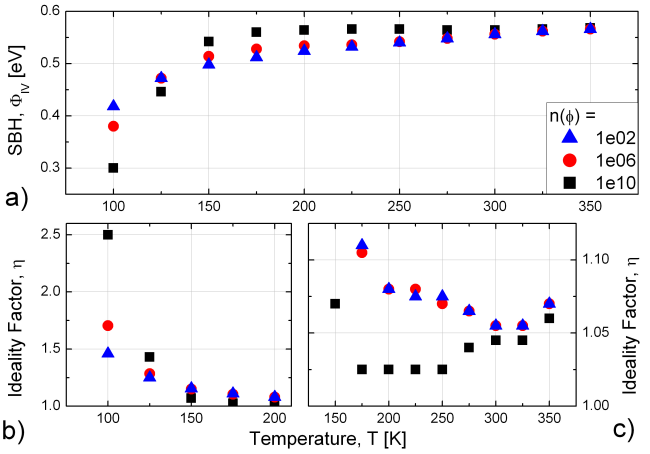


FIG. 10. The results of conventional SBH (a) and ideality factor (b and c) extraction from the simulations of Figure 9. The ideality factor results are split into two to illustrate the divergence problems of the larger value of $n[\phi_{\max}]$ in c).

### E. The extraction of $n[\phi_{\max}]$ from the real diodes.

Figure 9 displays the impact of $n[\phi_{\max}]$ on the IVT response. To complete the picture of the four diodes in light of the temperature dependent parameters within the Tung model, we here attempt to extract values of $n[\phi_{\max}]$ for each of them. However, to do this, we need to compare the patch barrier height activation rate ($F\left[T;T_P^0,\sigma_T^2\right]$), which we can extract from Figure 6a, to the initial Gaussian distribution of minimum patch barrier heights ($F\left[\phi;\Phi_P^0,\sigma_\phi^2\right]$). So, a technique is needed to generate $\Phi_P^0$ from the original Tung model.

Referring back to Equations A8 and A9, they show how the background current is modelled in parallel with the patch current. The patch current is modelled at every temperature and voltage interval as a single barrier height ($\Phi_p$), where $\Phi_p\left[T,V\right]=\Phi_B^0-\alpha_2$. This current passes through an area $AC_p$ which is proportional to $C_1$, but due to the pinch-off of the patches, it is also temperature and voltage dependent as dictated by Equations A10, A11 and A13. Therefore, with the data extracted from the models, presented in Figure 5, we can plot $C_p$ against $\Phi_p$ at every temperature and voltage interval. a-d) of Figure 11 shows this data for the four diodes, it can be seen that for a constant voltage, a CDF with a mean SBH $\Phi_{p,V}^0$ and a standard deviation $\sigma_{\phi,V}$ can easily be fit to this data.

Considering just the 0-volt distributions of Figure 11 a-d), they are reminiscent of the Gaussian barrier height distributions within, for example, Werner and Guttler's paper[13], where the SBH distribution is described without the rather abstract patch parameter, $\gamma$, so potentially breaking the link between the barrier height distribution and the $R_0$ distribution. However, here, the data has originated from inhomogeneous diodes with non-linearities and double bumps, something that other techniques[13,22] cannot achieve. If we presume that the 0-volt CDF approximates the initial Gaussian distribution of patches of Equation 5, then we can enter the mean barrier heights $\Phi_{p,0}^0$ and $T_p^0$ into Equation 4 in order to approximate a value for $n[\phi_{\max}]$ for each diode. Hence in Table II, the values of $\Phi_{p,0}^0$ are listed along with the resulting values of $n[\phi_{\max}]$ for each diode. Unsurprisingly, and as predicted by the model of Figure 9, the Nb diode, with its significant inhomogeneity, has the greatest saddle-point carrier concentration with $n[\phi_{\max}]=5.74\times10^{14}$, whilst the value for the NiV is exceptionally low at $n[\phi_{\max}]=5.66\times10^{-1}$. The value for the Ti diode proved it to be more homogeneous that the Cr diode, the values respectively being $n[\phi_{\max}]=4.51\times10^4$ and $n[\phi_{\max}]=2.28\times10^8$.

Finally, Figure 11 gives us the opportunity to observe the voltage dependencies within the Tung model. In Figure 11d, the linear reduction of $\sigma_{\phi,V}$ is caused by the low barrier height patches being pinched-off, the result of a voltage dependent saddle point[9,11]. In Figure 11e, the

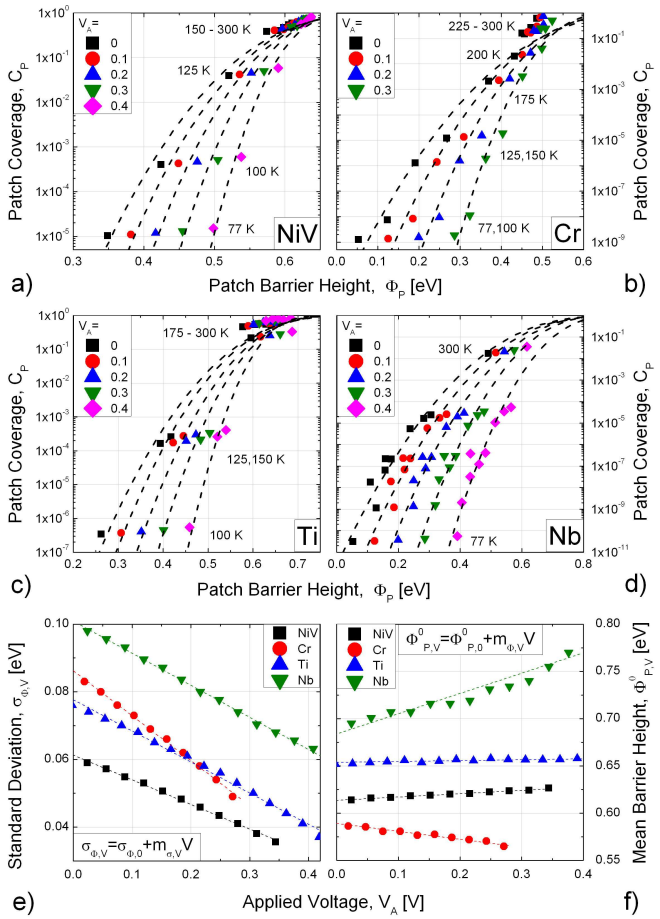


FIG. 11. a-d) are plots of the temperature and voltage dependent parameters that are used to model the patch current of the diodes of Figure 5, with the patch coverage $C_p$ plotted against the patch SBH $\Phi_p$. CDFs are fitted to the parameters of like voltage. e) and f) show how the CDF parameters vary with voltage.

mean barrier height, $\Phi^0_{p,V}$, of the more homogeneous Cr and NiV diodes does not particularly vary with voltage fluctuation, however, the Nb diode clearly shows some dependence. Both parameters appear to have a linear voltage dependency allowing us to apply a simple line of best fit to this data given the equations in the Figure. Table II summarises the voltage dependencies for the four diodes.

### F. The validity of the Tung model

The Tung model has been shown in this paper to reasonably reconstruct ideality factors greater than one, their inverse dependence on temperature, the apparent temperature dependence of the SBH, and the shape of the double bumps. However, there are still flaws in the model. Indeed, the accuracy of the model at the lowest temperatures, seen in Figure 5 and quantified using the coefficient of determination in Figure 6d, shows that though the lower part of the double bump is often accurately reproduced, the upper part of the double bump is not. This is due to the divergence at low temperatures of the two current paths built into the model. The current passing through the patches (governing the lower part of the curves) can be well manipulated by the fitting parameters, but the current passing through $I_{BG}$ ($I_{BG} = AA^*T^2 \exp\left(-\beta\Phi^0_B\right)(\exp\left[\beta V\right]-1)$), which will become dominant as the small number of available patches saturate, is modelled as a perfect diode without an ideality factor. This leads to the slopes within the simulations that, at low temperature and increased voltage, are too steep compared to the real data.

The divergence problem is most keenly observed in the simulation of Figure 9c, where a large $n[\phi_{\max}]$ was expected to produce a profile similar to that of the poorest interfaces, such as the Nb diode. However, one can see in the resulting profile that the two parallel current paths no longer interact, leaving an almost ideal set of IV profiles at high temperature (see the inset of Figure 9c), before the patch current becomes dominant at low temperature causing the double bumps and high ideality factors. This explains why the parameters of the Nb diode, especially $\sigma_\gamma$, were so different from the more homogeneous NiV and Ti diodes, each of which were well represented by the simulations of Figure 9a or b due to the two current paths largely overlapping to produce the inverse temperature-ideality factor dependence. Instead, the Nb IVT profile could only be modelled with the Tung Equations using a $\sigma_\gamma$ profile that increased with temperature.

Over a wide temperature range, the Tung model very accurately replicates the inverse temperature-ideality factor dependence, however, given the problems with divergence, it seems unlikely that this model in its current form will be able to exactly replicate the I-V profiles with significant double bumps, especially over an entire temperature range. At the heart of the problem is the complexity of competing mechanisms within a single interface. For instance, the Tung model of Equation A8 assumes that perhaps a single defect or inhomogeneity causes a perfect Gaussian distribution of patch barrier heights across the entire interface, the centre of the Gaussian being a single average background barrier height. It becomes easy to imagine that in reality, multiple non-linearities (perhaps surface roughness, dirt and/or trapped interfacial charge for instance) could lead to quite a different distribution of barriers, that might effect the interface much more locally, perhaps even adding in further parallel conduction paths or changing the shape of the patch distribution. Such a modification would have to include the divergence necessary to model the double bumps whilst retaining some influence on the ideality factor as the background current begins to dominate.

## IV. CONCLUSIONS

A study of the temperature dependencies inherent within the Tung model was presented. The aim of the work was to produce a model that could better reproduce the non-linearities present in $\log(I) - V$ plots, over a wide temperature range, hence improving our ability to predict the behaviour of real metal-silicon interfaces. In doing so we have presented both the strengths and weaknesses of the original model and made suggestions as to how the previously unexplored temperature dependencies within the model may be interpreted.

In particular, four silicon Schottky diodes were modelled, a comparatively homogeneous NiV diode, a Ti and a Cr diode displaying low temperature inhomogeneity, and a Nb diode displaying double bumps right up to room temperature. A semi-automated implementation of Tung's electron transport model was shown to generate accurate fits, though we documented some divergence problems at low temperature, and with extremely inhomogeneous interfaces. To achieve the fits, the three fitting parameters had to be individually optimised at every temperature interval, revealing a significant temperature dependence in each of them. This included the parameter $C_1$, which was thought to represent the total number of patches at an interface irrespective of temperature. However, $C_1$ was shown to increase exponentially with temperature, such that it fit a normal cumulative density function (CDF) with a mean temperature, and a corresponding standard deviation. We therefore suggest that $C_1$ is better defined as the number of *active* patches at a given temperature, whose saddle point is equal to or less than the energy that a conduction band electron may attain. In investigating this further, a link to interfacial homogeneity was found; we showed that the parameter $n_\phi$, the carrier concentration at the minimum saddle energy, could control the degree of non-linearity (high ideality factors and double bumps) present within a full I-V-T profile. Furthermore, for each of the diodes tested in this paper, a value of $n_\phi$ was estimated using a Gaussian SBH distribution extracted from the original model. The comparatively homogeneous NiV diode was shown to have a carrier concentration at $\phi_{\max}$ many orders of magnitude less than that of the inhomogeneous Nb diode. Finally, in a review of the model, the problems of divergence at low temperature were explained to be inherent due to the simplification of an interface that will contain competing defects and inhomogeneities.

Peter Gammon would like to gratefully acknowledge the financial support from the Royal Academy of Engineering. This work was supported by EPSRC grant EP/G060940/1, Nanostructured Functional Materials for Energy Harvesting.

### Appendix A: The Tung Model

According to Tung's model of "Electron transport at metal-semiconductor interfaces"[9], two components contribute to the current across a metal-semiconductor interface. That from the background current, $I_{BG}$, is modelled as a homogeneous interface, as a current passing over a uniform barrier height, $\Phi_B^0$, via thermionic emission (Equation 1). This occurs in parallel with a second current that passes over the many inhomogeneous, voltage dependent patches of varying barrier height. The individual patches are presumed circular with a radius, $R_0$, each with a potential "depth", $\Delta$, from $\Phi_B^0$[21]. Tung[9] defined a patch parameter, $\gamma$, that encompassed both of these parameters such that $\gamma = 3(\Delta R_0^2/4)^{1/3}$. $\gamma$ can be described by a probability density function (PDF), $P[x]$, which, in general is described by

$$P[x] = \int_{-\infty}^{\infty} f[x;\mu,\sigma^2] \tag{A1}$$

$$= \frac{1}{\sigma\sqrt{2\pi}} \int_{-\infty}^{\infty} \exp\left(-\frac{(x-\mu)^2}{2\sigma^2}\right) dx, \tag{A2}$$

where $\sigma$ is the standard deviation, and $\mu$ the mean of the variable x. Specifically for the patch parameter, a PDF is defined, $P[\gamma]$, and hence, given a mean value of 0, the distribution is defined as,

$$f[\gamma;\sigma_\gamma^2] = \frac{1}{\sigma_\gamma\sqrt{2\pi}} \exp\left(-\frac{\gamma^2}{2\sigma_\gamma^2}\right). \tag{A3}$$

The current passing through a single patch was defined[9] taking into account the pinch-off effect on the low SBHs, and the voltage dependency of the saddle point:

$$I_{\text{patch}}[\gamma,V] = A_{\text{eff}} A^* T^2 \exp\left(-\beta\left[\Phi_B^0 - \frac{\gamma V_{bb}^{1/3}}{\zeta^{1/3}}\right]\right) \times (\exp[\beta V] - 1) \tag{A4}$$

where, $\zeta = \epsilon_s/qn_{no}$, $V_{bb} = \Phi_B^0 - V_n - V$, $\epsilon_s$ is the permittivity of the semiconductor and $V_n$ the energy difference between the Fermi level and the conduction band. $A_{\text{eff}}$ is the localised effective area of a single patch, a temperature dependent variable defined[9,10,21] as,

$$A_{\text{eff}} = \frac{4\pi\gamma\zeta^{2/3}}{9\beta V_{bb}^{2/3}} \tag{A5}$$

At 300 K, the number of free carriers within the conduction band, $n_{no}$, may all be presumed to be from the phosphorous dopants ($N_D = 1\times10^{16}$ cm$^{-3}$), with the intrinsic carrier concentration ($n_i$) being negligible (less than $1\times10^{10}$ cm$^{-3}$). However, dopant freeze out at the lower temperatures does have to be considered. Hence,

from Sze[26], $n_{no}$ was found by solving graphically for the Fermi level energy ($E_F$) given that,

$$n_{no} = N_C \exp\left(-\frac{E_C - E_F}{kT}\right) \tag{A6}$$

$$\approx \frac{N_D}{1 + 2\exp\left[\left(E_F - E_D\right)/kT\right]} \tag{A7}$$

where $N_D$ is the density of the dopants, $N_C$ is the density of states in the conduction band, $E_C$ is the lower conduction band edge and $E_D$ the phosphorous donor energy, which lies 0.046 eV below $E_C$[26]. Along with $n_{no}$, $N_C$ was also considered temperature dependent, as was $E_F$ and $V_n$, with temperature related equations for each found in[26].

The total current passing through the interface is found by combining Equations 1, A3, A4 and A5,

$$I = C_1 A \int_{-\infty}^{\infty} f[\gamma; \sigma_\gamma^2] I_{\text{patch}}\left[\gamma, V\right] \, \mathrm{d}\gamma + I_{BG}\left[V\right] \tag{A8}$$

$$= AA^* T^2 \exp\left(-\beta\Phi_B^0\right)\left(\exp\left[\beta V\right] - 1\right) \times \left\{1 - C_p + C_p \exp\left(\beta\alpha_2\right)\right\} \tag{A9}$$

where $C_1$ is the areal density of patches with units of $\mathrm{cm}^{-2}$ and $C_p$ is the percentage area taken up by low barrier patches, with

$$C_p \approx C_1 A_{\text{eff}} = \alpha_1\alpha_3. \tag{A10}$$

The values $\alpha_1$, $\alpha_2$ and $\alpha_3$ are temperature and voltage dependent variables given by,

$$\alpha_1 = \frac{2\pi C_1 \sigma_\gamma^2 \zeta^{1/3}}{9 V_{bb}^{1/3}}, \tag{A11}$$

$$\alpha_2 = \frac{\beta\sigma_\gamma^2 V_{bb}^{2/3}}{2\zeta^{2/3}}, \tag{A12}$$

$$\alpha_3 = 1 + \mathrm{erf}\left(\sqrt{\beta\alpha_2}\right), \tag{A13}$$

Although rewritten here, this is the same model adapted from Tung's original work[9] by Im et al[21], to reduce the contribution of the background current by the percentage area ($C_p$) taken up by low barrier patches. Within Equation A9, three fitting parameters need to be selected to model any given I-V response; $C_1$, $\sigma_\gamma$, and $\Phi_B^0$. The rest of Equations A9-A13 can be derived from fundamental constants, or from materials properties, which are often individually temperature or voltage dependent. The size of $C_1$ had to be limited (typically to a maximum of $1 \times 10^{12}$ $\mathrm{cm}^{-2}$) to prevent the fractional coverage, $C_P$ exceeding 1.

## Appendix B: The coefficient of determination.

The coefficient of determination is defined as,

$$R^2 = 1 - \frac{\sum_i \left(y_i - \overline{y}\right)^2}{\sum_i \left(y_i - f_i\right)^2} \tag{B1}$$

where for every point on the x-axis (the voltage-axis), $y_i$ is the experimental data point and $f_i$ the corresponding data point from the model. $\overline{y}$ is the average of all the experimental data points. Herein,

$$y_i = \log\left(I_{V,\text{Exp}}\right), \tag{B2}$$

$$f_i = \log\left(I_{V,\text{Fit}}\right), \tag{B3}$$

$$\overline{y} = \frac{1}{n}\sum_i^n \log\left(I_{V,\text{Exp}}\right). \tag{B4}$$

As a good fit could be $R^2 = 99.99\%$, throughout this paper the quality of fit is presented as a percentage, defined by $1 - R^2$, and hence 0% would be a perfect fit.


[1] B. Ozpineci and L. Tolbert, "Smaller, faster, tougher", *IEEE Spectrum*, **48**, 10 45 (2011).
[2] A. Fontserè , A. Pérez-Tomás, M. Placidi, J. Llobet, N. Baron, S. Chenot, Y. Cordier, J. C. Moreno, M. R. Jennings, P. M. Gammon, C. A. Fisher, V. Iglesias, M. Porti, A. Bayerl, M. Lanza and M. Nafra, *Nanotechnology* **23** 395204 (2012).
[3] M. Asif Khan, A. Bhattarai, J. N. Kuznia, and D. T. Olson, *Appl. Phys. Lett.* **63**, 1214 (1993).
[4] N. Miura, T. Nanjo, M. Suita, T. Oishi, Y. Abe, T. Ozeki, H. Ishikawa, T. Egawa and T. Jimbo, *Solid-State Elec.*, **48**, 5 689, (2004).
[5] P. M. Smith, *IEEE Transactions on Microwave Theory and Techniques* **44**, 12 2328 (1996).
[6] S. Heinze, J. Tersoff, R. Martel, V. Derycke, J. Appenzeller, and Ph. Avouris, **Phys. Rev. Lett. 89**, 106801 (2002).
[7] J. M. Luther, M. Law, M. C. Beard, Q. Song, M. O. Reese, R. J. Ellingson, and A. J. Nozik, *Nano Lett.* **10** 8 3488 (2008).
[8] X. Li, H. Zhu, K. Wang, A. Cao, J. Wei, C. Li, Y. Jia, Z. Li, X. Li and D. Wu, *Adv. Mater.*, **22** 2743 (2010).
[9] R. T. Tung, *Phys. Rev. B*, **45**, 13509 (1992).
[10] J. P. Sullivan, R. T. Tung, M. R. Pinto, and W. R. Graham, *J. Appl. Phys.*, **70**, 7403 (1991)
[11] R. T. Tung, *Mat. Sci. Eng.*, **35**, 1 (2001).
[12] P. M. Gammon, A. Pérez-Tomás, V. A. Shah, G. J. Roberts, M. R. Jennings, J. A. Covington, and P. A. Mawby *J. Appl. Phys.* **106**, 093708 (2009).
[13] J. H. Werner and H. H. Güttler, *J. Appl. Phys.* **69**, 1522 (1991).
[14] J. L. Freeouf, T. N. Jackson, S. E. Laux, and J. M. Woodall, *J. Vac. Sci. Technol.*, **21**, 2570 (1982).
[15] I. Ohdomari and K. N. Tu, *J. Appl. Phys.* **51**, 3735 (1980).
[16] D. Defives, O. Noblanc, C. Dua, C. Brylinski, M. Barthula and F. Meyer, *Mat. Sci. and Eng: B*, **61**, 395 (1999).
[17] B. J. Skromme, E. Luckowski, K. Moore, M. Bhatnagar, C. E. Weitzel, T. Gehoski and D. Ganser, *J. Elec. Mat.* **29**, 376 (2000).
[18] I. Nikitina, K. Vassilevski, A. Horsfall, N. Wright, A. G. O'Neill, S. K. Ray, K. Zekentes and C. M. Johnson, *Semicond. Sci. Technol.* **24**, 055006 (2009).
[19] D. J. Ewing, L. M. Porter, Q. Wahab, X. Ma, T. S. Sudharshan, S. Tumakha, M. Gao, and L. J. Brillson *J. Appl. Phys.* **101**, 114514 (2007).

[20]X. Ma,P. Sadagopan and T. S. Sudarshan *Phys. Stat. Sol. a* **203**, 643 (2006).
[21]H. J. Im, Y. Ding, J. P. Pelz and W. J. Choyke, *Phys. Rev. B*, **64**, 075310, (2001).
[22]F. Roccaforte, F. La Via, V. Raineri, R. Pierobon, and E. Zanoni, *J. Appl. Phys.*, **93**, 9137 (2003).
[23]D. Korucu, H. Efeoglu, A. Türüt,, and S. Altindal, *Mat. Sci. Semicond. Proc.*, **15**, 5 480 (2012)
[24]A. Bengi, S. Altindal, S. Özçelik and T. S. Mammadov, *Physica B*, 396, 22 (2007).
[25]P. M. Gammon, A. Pérez-Tomás, M. R. Jennings, V. A. Shah, S. A. Boden, M. C. Davis, S. E. Burrows, N. R. Wilson, G. J. Roberts, J. A. Covington, and P. A. Mawby *J. Appl. Phys.*, **107**, 124512 (2010).
[26]S. M. Sze and K. K. Ng, *Physics of Semiconductor Devices*, (Wiley, New York, 2007). Si Dopant and freeze out calculations: pp 23-26.
[27]D. K. Schroder, *Semiconductor Material and Device Characterization*, p. 158 (Wiley, New York, 1998).
[28]W. Mönch, *Electronic Properties of Semiconductor Interfaces*, (Springer, Berlin, 2004).
[29]R. T. Tung, *Mat. Sci. Eng.*, **35**, 1 (2001).